Spectral diagnostic capabilities of Solar-B EIS

G. Del Zanna [a,b] H.E. Mason [a]

[a] *DAMTP, University of Cambridge, Wilberforce Road, Cambridge, CB3 0WA UK*
[b] *MSSL, University College London, Holmbury St. Mary RH5 6NT UK*

Abstract

In this paper we provide simulated intensities for Solar-B EIS to aid in the scientific planning for Solar-B. These simulations are obtained with the latest atomic data and EIS response functions. We also report on our progress in reviewing and benchmarking atomic data for the Fe coronal ions, that are of particular importance for spectral and instrument calibration purposes. We highlight the most prominent lines that can be used for plasma diagnostics.

Key words: Solar corona, spectral diagnostics, atomic data for astrophysics

1 Introduction

Solar-B is the follow up to the highly successful Japanese satellite YOHKOH (Solar-A). It is an international collaboration between Japan (ISAS), the USA (NASA), the UK (PPARC), ESA and Norway. The launch is planned for August 2006. The Solar-B payload comprises three instruments: the Solar Optical Telescope (SOT), the X-ray Telescope (XRT) and the EUV Imaging Spectrometer (EIS). The main science goals of Solar-B are:

- to determine the mechanisms responsible for heating the corona in active regions and the quiet Sun
-to determine the mechanisms responsible for transient phenomena, such as flares and CMEs
- to investigate the processes responsible for energy transfer from the photosphere to the corona.

The instruments on Solar-B will work as an integrated observatory, each instrument providing complementary observations. EIS is designed to determine the physical parameters of features in the solar atmosphere (temperature

distribution, density, flows etc). The wavelength bands covered by EIS have been carefully chosen to cover a wide temperature range, from chromospheric (He II) to flare (Fe XXIV) temperatures.

EIS has an off-axis paraboloid design, with multilayer toroidal gratings. Two wavelength bands will be covered: a short-wavelength (SW: 163–209 Å) and a long-wavelength (LW: 242–289 Å) one (James,A. priv. comm.).

This wavelength range was partially covered by the SOHO CDS grazing incidence spectrometer (GIS). Fig. 1 shows an example spectrum of an active region. Despite the low spectral resolution, the GIS spectra have been useful to study the emission from a wide range of solar features (Del Zanna, 1999).

The angular resolution of EIS is 2", with a field of view of 6' x 8.5'. The spectral resolution will enable the determination of Doppler shifts greater than 3km/s and non thermal line widths greater than 20km/s. Four different slit/slot selections are available (1", 2", 40" and 250"). In this paper we concentrate on predicting which spectral lines will be useful for different solar conditions (quiet Sun, active regions and solar flares).

More details of the EIS instrument and science planning can be found on the web-pages for the EIS PI group at the Mullard Space Science Laboratory (`http://www.mssl.ucl.ac.uk/www_solar/solarB/`). Certain data products (intensity, Doppler shift and line width maps) will be routinely provided. Many specific observing sequences are being planned to cover a wide range of topics including: quiet sun transient brightenings; active region heating; flare trigger and dynamics; CME onset and coronal hole boundaries.

2 EIS - Simulated Spectra

The CHIANTI atomic database and software is now extensively used by the international solar physics community (`www.chianti.rl.ac.uk`). Version 4.2 was released last year Young et al. (2003). We use CHIANTI as the basis for the simulations in this paper, supplemented by recent atomic data: Fe X, collisional and radiative data from (Del Zanna et al., 2004); Fe XII, collisional data from Storey et al. (2005) and *A*-values from Del Zanna and Mason (2005b); Fe XXIII, collisional data from Chidichimo et al. (2005) and *A*-values from Del Zanna et al. (2005a); Fe XXIV, data described in Del Zanna (2005).

In Figs.2,3,4 we show simulated spectra for the quiet Sun, an active region and a solar flare respectively. The CHIANTI intensities have been fed through the EIS response function to predict spectral intensities for each wavelength band. One can see immediately from these figures which spectral lines are

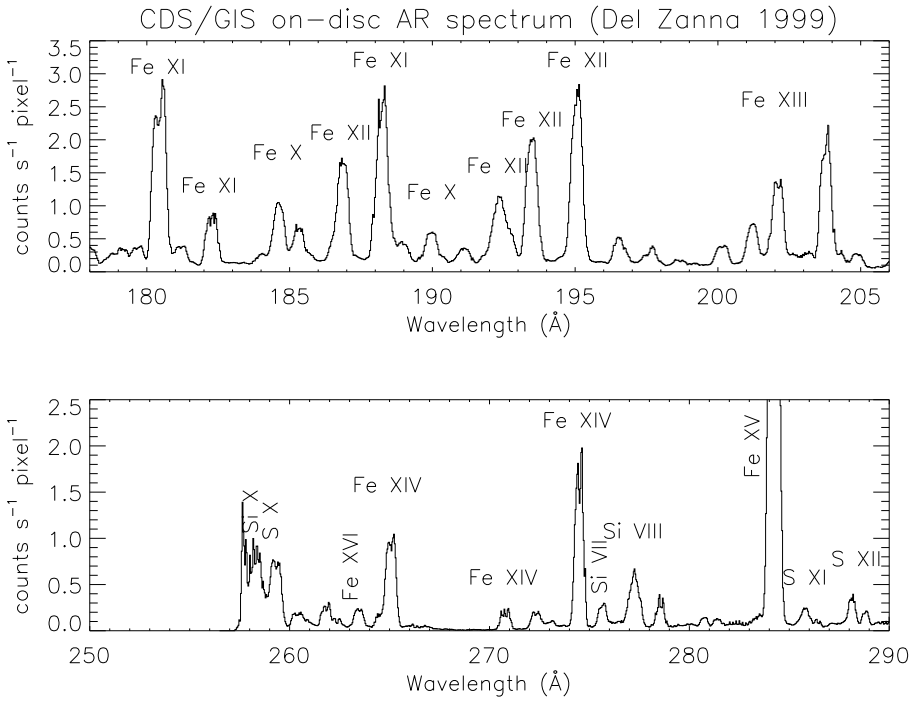

Fig. 1. SOHO CDS/GIS spectra of an on-disc active region, in the EIS spectral ranges.

available for diagnostic purposes. In Tables 1,2 we provide total count rates (detected counts/s) for one EIS pixel (1") and for the prominent lines in the various regimes, together with line identifications. The wavelengths, taken from CHIANTI or the cited literature, are mostly based on observations. The temperatures indicated in the Tables are 'effective values', i.e. are averaged temperatures weighted by the emission measure distribution, and indicate where the bulk of the observed emission comes from (note that this might depart from the temperature of maximum ion fraction).

We have used the EIS effective areas available under SolarSoft [1] as of August 2004 (files `EIS_EffArea_A,B.002`). These values are close to those recently measured during the ground calibration (Culhane,J.L., priv. comm.).

For the simulation, we have used three differential emission measures (DEM). For the average quiet Sun, we have used a DEM obtained from an extensive CDS NIS,GIS dataset taken in 1997 described in Andretta et al. (2003) and obtained with the in-flight calibration of Del Zanna et al. (2001). This represents a mid-cycle quiet Sun. The simulation was calculated at a constant density of 5 10^8 cm^{-3}. As an example of an active region spectrum, we have used a DEM obtained by Del Zanna (1999) from the well-known average SERTS-89 spectrum (Thomas and Neupert, 1994). The simulation was calcu-

[1] http://www.lmsal.com/solarsoft/

lated at a constant density 3 10^9 cm^{-3}. For the flare, we have chosen a DEM obtained by Dere and Cook (1979) from a Skylab observation of an M2 flare. The simulation was calculated at a constant density 10^{11} cm^{-3}

In all cases, photospheric abundances and the ionization fractions of Arnaud and Rothenflug (1985) were adopted. This is because, in the first two cases, they were adopted to obtain the DEM. Readers should be aware that the predicted count rates should be considered order-of-magnitude figures, not only because of the large solar variability in most lines, but also because of the anomalous behaviour of the spectral lines of many ions. This anomalous behaviour, most pronounced for He lines and for those of the Li and Na isoelectronic sequences (cf. Del Zanna et al., 2002) means that line intensities can be under- or over-estimated by large factors. For the bright He II, correction factors based on observations have been applied. For the quiet Sun case, a correction factor of 30 has been adopted (cf. Andretta et al., 2003), while for the AR and flare cases a factor of 15 was used.

3 EIS Spectroscopic Diagnostics

Table 3 lists some of the density-sensitive line ratios available with EIS.

For the quiet Sun, a range of iron ions (Fe VIII - Fe XIII) will be seen in the SW band. Additional iron ions (Fe XIV and Fe XV) will be observed in the LW band, as well as lines from Si VII,VIII,X, S X,XI. This provides a good coverage over upper transition-region and coronal temperatures. The strongest line by far is from He II (256 Å). The cool lines from Fe VIII, Si VII and Mg VII should be very useful for studying the upper transition region and cool features such as polar plumes (Del Zanna et al., 2003) or the 'cool' active region loops first characterised by Del Zanna and Mason (2003). There are some lines from lower temperature transition region ions Mg V (276 Å) and Mg VI (270 Å), but these may be too weak to observe. Details of EIS studies are given on the EIS web pages. Studies of quiet Sun brightenings are listed in the 'EIS Initial science Plan' and also under 'EIS studies'. With the 1" slit the exposure time may need to be up to 50s, which does somewhat restrict studies of short term behaviour.

The lines useful for density diagnostic purposes are relatively weak and long exposure times will be needed. For example, with the 1" slit, the exposure time will need to be at least 100s to get good statistics for the Si X 258.4/261.0 Å density-sensitive diagnostic. The Fe XII 196.6/195.1 Å is also a good density-sensitive diagnostic (cf. Del Zanna and Mason, 2005b) for EIS. The Fe X 257.2/190.0 Å will be an excellent diagnostic (cf. Del Zanna et al., 2004) but only for high densities. Unfortunately, the important Fe IX 242, 245 Å

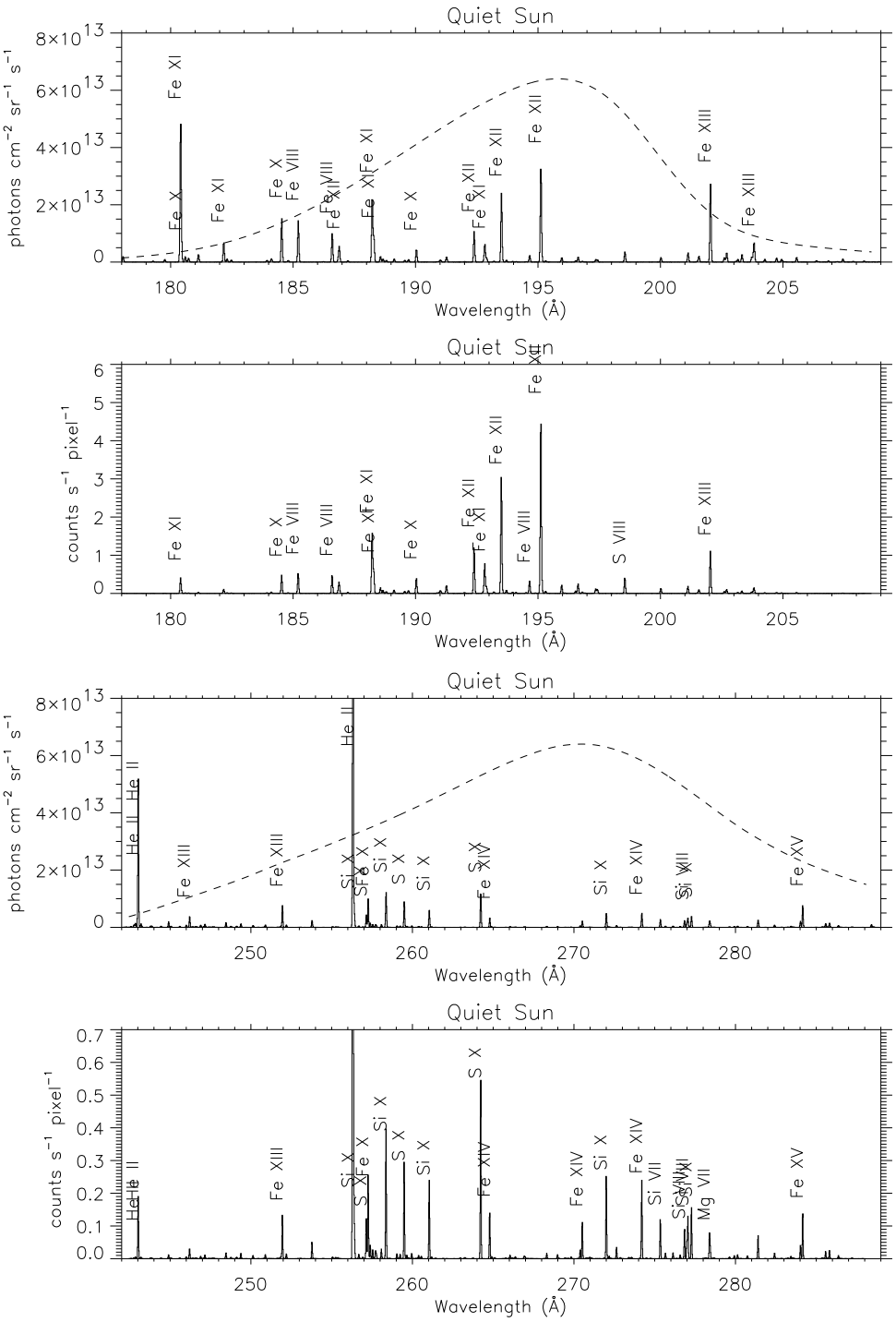

Fig. 2. Simulated spectra in the Solar-B EIS bands for typical quiet Sun conditions. The top spectra show the simulated spectra. The dashed line indicates the sensitivity (scaled) of the EIS band. The bottom spectra simulate the observed count rate spectra for 1" region of the Sun.

Table 1
Total detected counts/s (1" pixel) for the prominent lines in the short-wavelength band - quiet Sun case (QS), active region (AR) and an M2 flare (Flare).

Ion	λ (Å)	Transition	log T	QS	AR	Flare
Fe X	174.531	$3s^2\ 3p^5\ ^2P_{3/2}$ - $3s^2\ 3p^4\ (^3P)\ 3d\ ^2D_{5/2}$	6.0	0.13	0.23	
Fe X	177.240	$3s^2\ 3p^5\ ^2P_{3/2}$ - $3s^2\ 3p^4\ (^3P)\ 3d\ ^2P_{3/2}$	6.0	0.22	0.39	
Fe XI	180.408	$3s^2\ 3p^4\ ^3P_2$ - $3s^2\ 3p^3\ (^4S)\ 3d\ ^3D_3$	6.1	0.99	2.1	18.
Fe XI	182.169	$3s^2\ 3p^4\ ^3P_1$ - $3s^2\ 3p^3\ (^4S)\ 3d\ ^3D_2$	6.1	0.27	0.97	15.
Ca XIV	183.460	$2s^2\ 2p^3\ ^4S_{3/2}$ - $2s\ 2p^4\ ^4P_{1/2}$	6.4		0.85	
O VI	184.117	$1s^2\ 2p\ ^2P_{3/2}$ - $1s^2\ 3s\ ^2S_{1/2}$	6.4		0.75	27.
Fe X	184.537	$3s^2\ 3p^5\ ^2P_{3/2}$ - $3s^2\ 3p^4\ (^1D)\ 3d\ ^2S_{1/2}$	6.0	1.2	2.3	29.
Fe XI	184.803	$3s^2\ 3p^4\ ^1D_2$ - $3s^2\ 3p^3\ (^2D)\ 3d\ ^1D_2$	6.2		0.48	25.
Fe VIII	185.213	$3p^6\ 3d\ ^2D_{5/2}$ - $3p^5\ 3d^2\ (^3F)\ ^2F_{7/2}$	6.0	1.3	3.7	96.
Fe VIII	186.599	$3p^6\ 3d\ ^2D_{3/2}$ - $3p^5\ 3d^2\ (^3F)\ ^2F_{5/2}$	6.0	1.3	3.5	91.
Ca XIV	186.610	$2s^2\ 2p^3\ ^4S_{3/2}$ - $2s\ 2p^4\ ^4P_{3/2}$	6.4		3.8	29.
Fe XII	186.854	$3s^2\ 3p^3\ ^2D_{3/2}$ - $3s^2\ 3p^2\ (^3P)\ 3d\ ^2F_{5/2}$	6.1	0.14	1.8	55.
Fe XII	186.887	$3s^2\ 3p^3\ ^2D_{5/2}$ - $3s^2\ 3p^2\ (^3P)\ 3d\ ^2F_{7/2}$	6.1	0.69	4.8	87.
Fe XXI	187.924	$2s^2\ 2p^2\ ^1D_2$ - $2s\ 2p^3\ ^3D_1$	7.0			$2.4\ 10^2$
Ar XIV	187.969	$2s^2\ 2p\ ^2P_{3/2}$ - $2s\ 2p^2\ ^2P_{3/2}$	6.4		2.0	36.
Fe XI	188.232	$3s^2\ 3p^4\ ^3P_2$ - $3s^2\ 3p^3\ (^2D)\ 3d\ ^3P_2$	6.1	4.3	9.6	91.
Fe XI	188.299	$3s^2\ 3p^4\ ^3P_2$ - $3s^2\ 3p^3\ (^2D)\ 3d\ ^1P_1$	6.1	1.6	3.5	40.
S XI	188.675	$2s^2\ 2p^2\ ^3P_1$ - $2s\ 2p^3\ ^3S_1$	6.2	0.22	7.0	36.
Fe XI	189.129	$3s^2\ 3p^4\ ^3P_1$ - $3s^2\ 3p^3\ (^2D)\ 3d\ ^3P_1$	6.1	0.22	0.96	21.
Fe X	190.037	$3s^2\ 3p^5\ ^2P_{1/2}$ - $3s^2\ 3p^4\ (^1D)\ 3d\ ^2S_{1/2}$	6.0	1.0	2.0	25.
S XI	191.266	$2s^2\ 2p^2\ ^3P_2$ - $2s\ 2p^3\ ^3S_1$	6.2	0.54	18.	90.
Ar XIV	191.404	$2s^2\ 2p\ ^2P_{3/2}$ - $2s\ 2p^2\ ^2P_{1/2}$	6.4		2.6	28.
Fe XXIV	192.028	$1s^2\ 2s\ ^2S_{1/2}$ - $1s^2\ 2p\ ^2P_{3/2}$	7.0		0.21	$5.9\ 10^4$
Fe XII	192.394	$3s^2\ 3p^3\ ^4S_{3/2}$ - $3s^2\ 3p^2\ (^3P)\ 3d\ ^4P_{1/2}$	6.1	3.3	12.	85.
O V	192.797	$2s\ 2p\ ^3P_1$ - $2s\ 3d\ ^3D_2$	5.4			$1.3\ 10^2$
Ca XVII	192.819	$2s^2\ ^1S_0$ - $2s\ 2p\ ^1P_1$	6.7		3.4	$1.6\ 10^3$
O V	192.904	$2s\ 2p\ ^3P_2$ - $2s\ 3d\ ^3D_3$	5.4	0.24	0.28	$3.0\ 10^2$
Fe XII	193.509	$3s^2\ 3p^3\ ^4S_{3/2}$ - $3s^2\ 3p^2\ (^3P)\ 3d\ ^4P_{3/2}$	6.1	7.6	29.	$1.9\ 10^2$
Ca XIV	193.866	$2s^2\ 2p^3\ ^4S_{3/2}$ - $2s\ 2p^4\ ^4P_{5/2}$	6.4		16.	$1.2\ 10^2$
Ar XIV	194.396	$2s^2\ 2p\ ^2P_{1/2}$ - $2s\ 2p^2\ ^2S_{1/2}$	6.4		8.1	56.
Fe XII	195.119	$3s^2\ 3p^3\ ^4S_{3/2}$ - $3s^2\ 3p^2\ (^3P)\ 3d\ ^4P_{5/2}$	6.1	12.	46.	$3.2\ 10^2$
Fe XII	195.179	$3s^2\ 3p^3\ ^2D_{3/2}$ - $3s^2\ 3p^2\ (^1D)\ 3d\ ^2D_{3/2}$	6.1	0.17	2.1	66.
Fe XIII	196.540	$3s^2\ 3p^2\ ^1D_2$ - $3s^2\ 3p\ 3d\ ^1F_3$	6.2	0.16	6.2	$2.6\ 10^2$
Fe XII	196.640	$3s^2\ 3p^3\ ^2D_{5/2}$ - $3s^2\ 3p^2\ (^1D)\ 3d\ ^2D_{5/2}$	6.1	0.60	4.2	83.
Fe XIII	197.433	$3s^2\ 3p^2\ ^3P_0$ - $3s^2\ 3p\ 3d\ ^3D_1$	6.2	0.26	3.2	26.
S VIII	198.553	$2s^2\ 2p^5\ ^2P_{3/2}$ - $2s\ 2p^6\ ^2S_{1/2}$	6.0	0.82	2.3	58.
Fe XIII	200.022	$3s^2\ 3p^2\ ^3P_1$ - $3s^2\ 3p\ 3d\ ^3D_2$	6.2	0.33	6.6	67.
Fe XIII	202.044	$3s^2\ 3p^2\ ^3P_0$ - $3s^2\ 3p\ 3d\ ^3P_1$	6.2	2.8	12.	47.
Fe XIII	203.798	$3s^2\ 3p^2\ ^3P_2$ - $3s^2\ 3p\ 3d\ ^3D_2$	6.2		2.2	23.
Fe XIII	203.828	$3s^2\ 3p^2\ ^3P_2$ - $3s^2\ 3p\ 3d\ ^3D_3$	6.2	0.32	6.8	67.
Fe XVII	204.654	$2p^5\ 3s\ ^1P_1$ - $2p^5\ 3p\ ^1S_0$	6.4		0.31	21.
Mn XXIII	206.902	$1s^2\ 2s\ ^2S_{1/2}$ - $1s^2\ 2p\ ^2P_{3/2}$	7.1			40.

Table 2
Total count rates for the prominent lines in the EIS long-wavelength band.

Ion	λ (Å)	Transition	log T	QS	AR	Flare
He II	243.026	1s ^{2}S$_{1/2}$ - 4p ^{2}P$_{3/2}$	4.9	0.33	0.49	3.6 10^2
He II	243.027	1s ^{2}S$_{1/2}$ - 4p ^{2}P$_{1/2}$	4.9	0.17	0.25	1.8 10^2
Ni XVII	249.178	3s^2 ^{1}S$_0$ - 3s 3p ^{1}P$_1$	6.4		4.0	16.
Fe XVI	251.063	3p ^{2}P$_{1/2}$ - 3d ^{2}D$_{3/2}$	6.4		2.0	17.
Fe XIII	251.956	3s^2 3p^2 ^{3}P$_2$ - 3s 3p^3 ^{3}S$_1$	6.2	0.35	3.3	26.
Fe XXII	253.170	2s^2 2p ^{2}P$_{3/2}$ - 2s 2p^2 ^{4}P$_{5/2}$	7.0			1.1 10^2
Fe XVII	254.868	2p^5 3s ^{3}P$_1$ - 2p^5 3p ^{1}S$_0$	6.4		0.44	30.
Fe XXIV	255.113	1s^2 2s ^{2}S$_{1/2}$ - 1s^2 2p ^{2}P$_{1/2}$	7.1			6.0 10^3
He II	256.317	1s ^{2}S$_{1/2}$ - 3p ^{2}P$_{3/2}$	4.9	7.0	13.	1.9 10^4
He II	256.318	1s ^{2}S$_{1/2}$ - 3p ^{2}P$_{1/2}$	4.9	3.5	6.5	9.7 10^3
Si X	256.366	2s^2 2p ^{2}P$_{1/2}$ - 2s 2p^2 ^{2}P$_{1/2}$	6.1	0.49	1.6	17.
S XIII	256.685	2s^2 ^{1}S$_0$ - 2s 2p ^{1}P$_1$	6.4		64.	3.9 10^2
S X	257.147	2s^2 2p^3 ^{4}S$_{3/2}$ - 2s 2p^4 ^{4}P$_{1/2}$	6.1	0.32	1.5	10.
Fe X	257.259	3s^2 3p^5 ^{2}P$_{3/2}$ - 3s^2 3p^4 (^{3}P) 3d ^{4}D$_{5/2}$	6.0	0.14	0.34	
Fe X	257.263	3s^2 3p^5 ^{2}P$_{3/2}$ - 3s^2 3p^4 (^{3}P) 3d ^{4}D$_{7/2}$	6.0	0.52	0.57	
Fe XIV	257.395	3s^2 3p ^{2}P$_{1/2}$ - 3s 3p^2 ^{2}P$_{1/2}$	6.2	0.10	3.5	22.
Si X	258.371	2s^2 2p ^{2}P$_{3/2}$ - 2s 2p^2 ^{2}P$_{3/2}$	6.1	1.0	4.9	63.
Ti XX	259.272	1s^2 2s ^{2}S$_{1/2}$ - 1s^2 2p ^{2}P$_{3/2}$	7.0			61.
S X	259.496	2s^2 2p^3 ^{4}S$_{3/2}$ - 2s 2p^4 ^{4}P$_{3/2}$	6.1	0.73	3.5	24.
Si X	261.043	2s^2 2p ^{2}P$_{3/2}$ - 2s 2p^2 ^{2}P$_{1/2}$	6.1	0.61	2.0	22.
Fe XVI	262.976	3p ^{2}P$_{3/2}$ - 3d ^{2}D$_{5/2}$	6.4		8.4	72.
Fe XXIII	263.765	2s^2 ^{1}S$_0$ - 2s 2p ^{3}P$_1$	7.1			2.2 10^3
S X	264.230	2s^2 2p^3 ^{4}S$_{3/2}$ - 2s 2p^4 ^{4}P$_{5/2}$	6.1	1.4	6.9	47.
Fe XIV	264.789	3s^2 3p ^{2}P$_{3/2}$ - 3s 3p^2 ^{2}P$_{3/2}$	6.2	0.39	17.	1.6 10^2
Mn XXIII	266.880	1s^2 2s ^{2}S$_{1/2}$ - 1s^2 2p ^{2}P$_{1/2}$	7.1			88.
Fe XVII	269.411	2p^5 3p ^{3}D$_2$ - 2p^5 3d ^{3}F$_3$	6.4		0.21	14.
Mg VI	270.390	2s^2 2p^3 ^{2}D$_{5/2}$ - 2s 2p^4 ^{2}P$_{3/2}$	5.8		0.42	65.
Fe XIV	270.521	3s^2 3p ^{2}P$_{3/2}$ - 3s 3p^2 ^{2}P$_{1/2}$	6.2	0.31	10.	65.
Fe XXI	270.566	2s^2 2p^2 ^{3}P$_2$ - 2s 2p^3 ^{5}S$_2$	7.0			1.5 10^2
Si X	272.005	2s^2 2p ^{2}P$_{1/2}$ - 2s 2p^2 ^{2}S$_{1/2}$	6.1	0.68	2.2	24.
Si VII	272.638	2s^2 2p^4 ^{3}P$_2$ - 2s 2p^5 ^{3}P$_1$	6.0	9.0 10^{-2}	0.40	16.
Fe XIV	274.204	3s^2 3p ^{2}P$_{1/2}$ - 3s 3p^2 ^{2}S$_{1/2}$	6.2	0.59	17.	63.
Si VII	275.353	2s^2 2p^4 ^{3}P$_2$ - 2s 2p^5 ^{3}P$_2$	6.0	0.33	1.3	48.
Mg V	276.582	2s^2 2p^4 ^{1}D$_2$ - 2s 2p^5 ^{1}P$_1$	5.4			55.
Si VIII	276.849	2s^2 2p^3 ^{2}D$_{3/2}$ - 2s 2p^4 ^{2}D$_{3/2}$	6.0	0.19	0.78	22.
Mg VII	276.993	2s^2 2p^2 ^{3}P$_1$ - 2s 2p^3 ^{3}S$_1$	6.0	0.13	0.54	19.
Si VIII	277.057	2s^2 2p^3 ^{2}D$_{5/2}$ - 2s 2p^4 ^{2}D$_{5/2}$	6.0	0.33	1.0	32.
Si X	277.277	2s^2 2p ^{2}P$_{3/2}$ - 2s 2p^2 ^{2}S$_{1/2}$	6.1	0.43	1.4	15.
Mg VII	278.392	2s^2 2p^2 ^{3}P$_2$ - 2s 2p^3 ^{3}S$_1$	6.0	0.20	0.80	28.
Cr XXII	279.744	1s^2 2s ^{2}S$_{1/2}$ - 1s^2 2p ^{2}P$_{1/2}$	7.1			1.2 10^2
Mg VII	280.744	2s^2 2p^2 ^{1}D$_2$ - 2s 2p^3 ^{1}P$_1$	5.9		0.27	20.
S XI	281.402	2s^2 2p^2 ^{3}P$_0$ - 2s 2p^3 ^{3}D$_1$	6.2	0.19	2.8	8.2
Fe XV	284.163	3s^2 ^{1}S$_0$ - 3s 3p ^{1}P$_1$	6.2	0.38	68.	3.0 10^2
S XI	285.822	2s^2 2p^2 ^{3}P$_1$ - 2s 2p^3 ^{3}D$_2$	6.4		2.5	11.
S XII	288.421	2s^2 2p ^{2}P$_{1/2}$ - 2s 2p^2 ^{2}D$_{3/2}$	6.4		7.0	15.

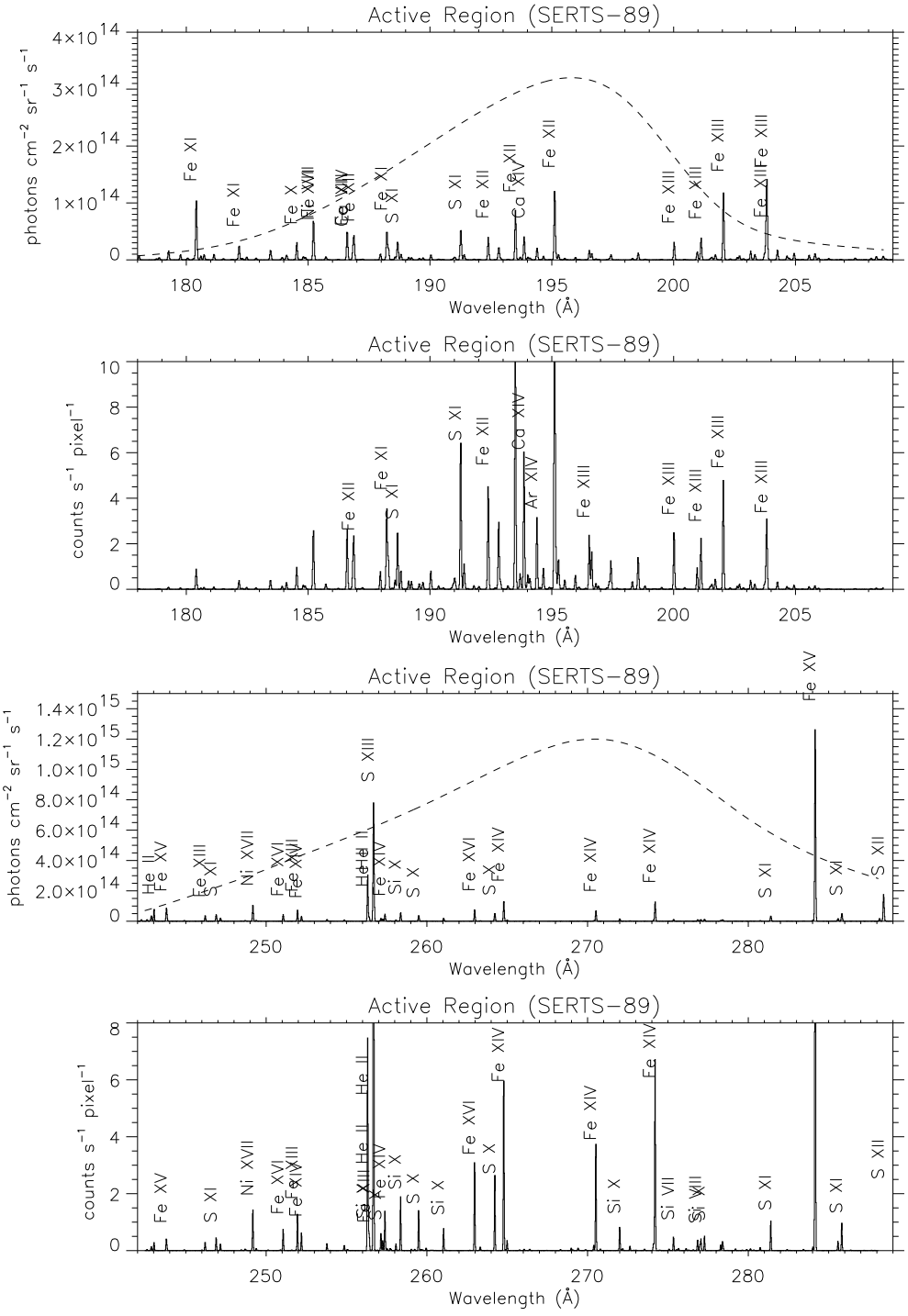

Fig. 3. Simulated spectra in the Solar-B EIS bands using a DEM from the SERTS-89 active region observation.

diagnostics (Storey et al., 2002) is just outside the EIS wavelength range.

In active region spectra, the number of lines, diagnostics and count rates dramatically improve. Lines from higher temperature ions such as Fe XIV,

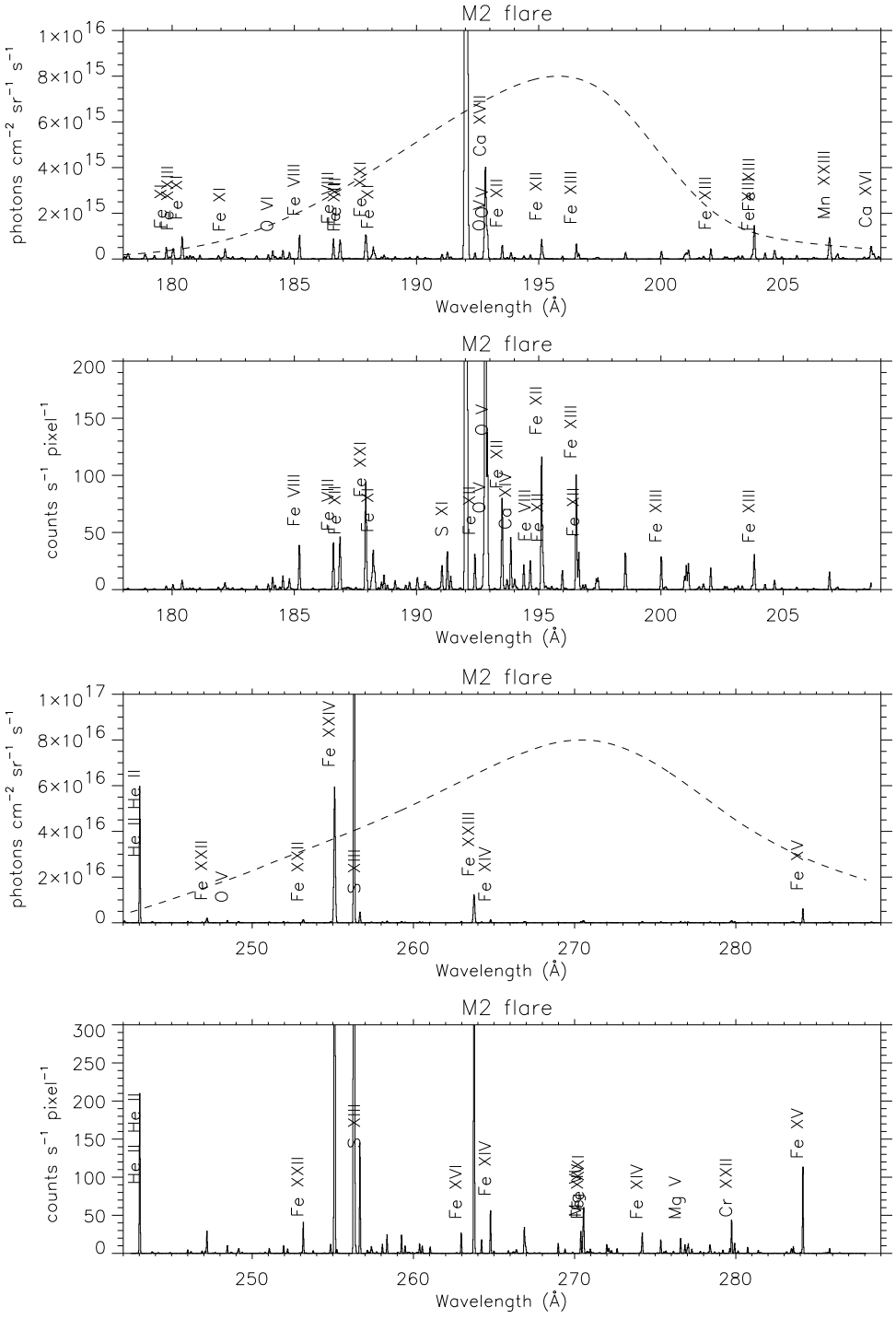

Fig. 4. Spectra in the Solar-B EIS bands simulating an M2 flare.

Fe XV, Fe XVI and S XI become prominent. On top of the lines previously mentioned, good diagnostics (at higher temperatures) will be obtained from many ions. For example, from a range of Fe XIII lines (the 196.5 or 203.8 Å against the 202.0 Å being the best), from S XI (e.g. 285.8/285.6 Å) and from a wide range of Fe XIV ratios, with relatively short exposure times (seconds).

Table 3
List of few density-sensitive line ratios available with EIS. The ion, the temperature of maximum abundance, the line ratios, and the approximate range (log N_e, cm^{-3}) of sensitivity are indicated. When multiple ratios can be used, they are indicated. For example, for Fe XII, the ratios of the 186.88 Å or 196.6 Å against any of the 192.3,193.5,195.1 Å lines is density-sensitive.

Ion	log T_{max}	λ (Å)	log N_e
Mg VII	5.8	280.7/278.4	9-11
Fe X	6.0	257.2/190.0	9-10
Si X	6.1	258.4/(261.0,272.0)	7-10
Fe XII	6.15	(186.88,196.6)/(192.3,193.5,195.1)	8-12
Fe XIII	6.2	(196.5,200.0,201.1,203.8)/202.0	9-11
S XI	6.3	(281.4,285.6)/285.8	7-10
Fe XIV	6.3	(257.4,274.2,270.5)/(264.7,252.2)	8.5-11

These diagnostics will prove crucial for a better understanding of the physics involved in the heating of the multi-million degrees loops and of the (yet) unresolved active region emission described in Del Zanna and Mason (2003).

The EIS wavelength range does not include any chromospheric lines. An absolute determination of flows is therefore problematic. However, flows can be measured relative to background emission as has been done successfully with SOHO/CDS data (cf. Pike and Mason 2002). With EIS it will be possible to study flows in active region cool and hot loops, and to distinguish different transient and wave-like phenomena. It should be possible to relate these events directly to magnetic flux changes. An integrated approach for hydrodynamic modelling is required taking account of non-equilibrium processes (cf. Bradshaw et al., 2004). It is essential to link such models with observable quantities.

It is anticipated that the 40" slot will be used frequently for small dynamic events, such as transient brightenings and micro-flares. The 40" slot has been chosen to minimise the spatial overlap in the direction of dispersion for the strongest spectral lines. It is also likely to be used to catch the initial stages of a flare.

For solar flares, EIS will observe a considerable number of spectral lines from high-temperature ions (such as Fe XVII,XXI-XXIV, Ca XV,XVII). EIS will accurately locate the sources of the high-temperature blue-shifted emission seen during the early stages of a flare. It is hoped that EIS will provide direct evidence for magnetic reconnection in flare-like phenomena.

4 Benchmarking atomic data for astrophysics

In order to reliably analyse the EIS spectra, we require accurate atomic data, particularly for the iron ions. In a series of papers, we have adopted a novel approach to benchmark atomic data for astrophysics. The main aim is to provide assessed sets of atomic data and identifications of the best spectral lines useful for plasma diagnostics or instrument calibration. The approach is observationally based, in the sense that it focuses only on the brightest spectral lines that are observed in normal astrophysical or laboratory plasmas. Existing atomic data are benchmarked against laboratory and solar observations. Whenever not available, new atomic data are calculated. All the spectral line identifications and wavelengths of each ion are reviewed in light of comparisons between theory and calibrated observations of line intensities and wavelengths. The presence of line blending for the most common cases is also discussed. The radiative data (energy levels, A values) are calculated with the SUPERSTRUCTURE program (Eissner et al. 1974; Nussbaumer and Storey 1978) and with semi-empirical Term Energy Corrections (TEC) that take into account the experimental energies. In turn, experimental energies are reviewed in light of all the available wavelength measurements, and the line identifications.

The first paper (Del Zanna et al., 2004) addressed Fe X, and provided new collisional and radiative data for this ion. The solar corona produces Fe X lines that will be observed by SOLAR-B EIS and that are useful for density diagnostics. This first paper also described the complexities of the benchmark method, and the limitations of the available theoretical and experimental data in general.

The second paper (Del Zanna and Mason, 2005b) dealt with Fe XII. Fe XII is another important ion because it produces strong spectral lines that will be observed by SOLAR-B EIS and that can be used both for plasma diagnostics and for instrument calibration. Long-standing discrepancies between theory and observations have always been present for Fe XII. In particular, in terms of the electron densities derived from line ratios. Only recently, Storey et al. (2005) performed a more complete electron scattering calculation which represent a significant improvement compared to all the previous calculations. The previous discrepancies have now, at last, been resolved.

Del Zanna and Mason (2005b) have benchmarked this new set of collisional data, identifying new lines and reviewing previous results and suggestions on the best spectral lines for electron density diagnostics. On-going benchmark work is on the other ions important for EIS, in particular Fe XI, Fe XIII. Fortunately, good atomic calculations are now available for many ions, thanks to the efforts of the Iron Project and R-max collaborations.

Acknowledgements

Support from PPARC is acknowledged.

References

Andretta, V., Del Zanna, G., Jordan, S. D., Mar. 2003. The EUV helium spectrum in the quiet Sun: A by-product of coronal emission? A&A 400, 737–752.

Arnaud, M., Rothenflug, R., Jun. 1985. An updated evaluation of recombination and ionization rates. A&AS 60, 425–457.

Bradshaw, S. J., Del Zanna, G., Mason, H. E., Oct. 2004. On the consequences of a non-equilibrium ionisation balance for compact flare emission and dynamics. A&A 425, 287–299.

Chidichimo, M. C., Del Zanna, G., Mason, H. E., & et al. 2005. Atomic data from the IRON Project LVI. Electron excitation of Be-like Fe XXIII. A&A , 430, 331.

Del Zanna, G., 1999. Ph.D. thesis, Univ. of Central Lancashire, UK.

Del Zanna, G., Bromage, B. J. I., Landi, E., Landini, M., Nov. 2001. Solar EUV spectroscopic observations with SOHO/CDS. I. An in-flight calibration study. A&A 379, 708–734.

Del Zanna, G., Landini, M., Mason, H. E., Apr. 2002. Spectroscopic diagnostics of stellar transition regions and coronae in the XUV: AU Mic in quiescence. A&A 385, 968–985.

Del Zanna, G., Bromage, B. J. I., Mason, H. E., Apr. 2003. Spectroscopic characteristics of polar plumes. A&A 398, 743–761.

Del Zanna, G., Mason, H. E., Aug. 2003. Solar active regions: SOHO/CDS and TRACE observations of quiescent coronal loops. A&A 406, 1089–1103.

Del Zanna, G., Berrington, K. A., Mason, H. E., Aug. 2004. Benchmarking atomic data for astrophysics: Fe X. A&A 422, 731–749.

Del Zanna, G., Chidichimo, M. C., & Mason, H. E. 2005a. Benchmarking atomic data for astrophysics: Fe XXIII. A&A , 432, 1137

Del Zanna, G., Mason, H. E., 2005b. Benchmarking atomic data for astrophysics: Fe XII. A&A , 433, 731.

Del Zanna, G., 2005. Benchmarking atomic data for astrophysics: Fe XXIV. A&A , in press

Dere, K. P., Cook, J. W., Apr. 1979. The decay of the 1973 August 9 flare. ApJ 229, 772–787.

Eissner, W., Jones, M., Nussbaumer, H., Nov. 1974. Techniques for the calculation of atomic structures and radiative data including relativistic corrections. Computer Physics Communications 8, 270–306.

Nussbaumer, H., Storey, P. J., Mar. 1978. The C III transition probabilities. A&A 64, 139–144.

Pike, C. D. and Mason, H. E., 2002. UV Spectroscopic Observations of Spray Ejecta from an X2 Flare. Sol. Phys. 206, 359.

Storey, P. J., Del Zanna, G., Mason, H. E., Zeippen,C., 2005. Atomic data from the IRON Project. LVIII. Electron impact excitation of Fe XII. A&A , 433, 717

Storey, P. J., Zeippen, C. J., Le Dourneuf, M., Nov. 2002. Atomic data from the IRON Project. LI. Electron impact excitation of Fe IX. A&A 394, 753–762.

Thomas, R. J., Neupert, W. M., Mar. 1994. Extreme ultraviolet spectrum of a solar active region from serts. ApJS 91, 461–482.

Young, P. R., Del Zanna, G., Landi, E., Dere, K. P., Mason, H. E., Landini, M., Jan. 2003. CHIANTI-An Atomic Database for Emission Lines. VI. Proton Rates and Other Improvements. ApJS 144, 135–152.